CrossMark

Optimization of precursor based on optical, structural and magnetic properties of Cu-doped ZnO nanoparticles

R. Sangeetha[1] · S. Muthukumaran[2] · M. Ashokkumar[2]

Abstract Cu doped ZnO nanoparticles were synthesized via co-precipitation method using different precursors like zinc chloride, zinc acetate and zinc nitrate. The crystallite structure, morphology and optical properties were discussed by X-ray diffraction, scanning electron microscopy and UV–visible photo-spectrometer for different precursors. The hexagonal structure was confirmed by X-ray diffraction. The calculated average crystallite size from XRD spectra was low for zinc chloride precursor (22.3 nm) and high for zinc nitrate precursor (26 nm). The strong and transparent behaviour in the visible region of the sample using zinc nitrate precursor is due to the existence of less defects and enhanced crystal size which leads to the industrial applications especially as transparent electrode. The reduction in strain and the better crystallinity effectively depress interstitial defects. The energy gap is varied between 3.65 and 3.75 eV, where zinc nitrate precursor has $E_g = 3.65$ eV (minimum) and zinc acetate precursor has $E_g = 3.75$ eV (maximum). The observed higher energy gap using zinc chloride precursor could be attributed to the poor crystallinity and also the formation of the new compound based on Cu and Zn. The low energy gap for zinc nitrate precursor can be attributed to the better crystallinity with increasing grain size. Change in luminescence intensity and magnetization were discussed based on the defects formation and structural parameters.

1 Introduction

ZnO is one of the important semiconductors with wide band gap (3.37 eV) [1]. Cu doping in ZnO, in general, has potential applications for green luminescence [2] and has also been used to make p-type ZnO [3]. The theoretical investigation shows that Cu doping can reduce the band gap of ZnO, leading to a red shift of luminescence [4], however, experimental evidences have been still absent. Initial doping of Cu into ZnO lattice increases the carrier concentration and further doping of Cu would be expected to create a secondary phase (CuO) and thereby decrease the carrier concentration [5]. Since, Cu related phases like CuO are observed in primary lattice system at higher concentrations [6, 7], in present investigation Cu doping concentration is limited to 0.04.

While the effect of surfactants, reaction conditions and solvents has been widely investigated, there is no information on the effect of precursors on the formation of Cu-doped ZnO nanoparticles. Although some studies have been published [1, 4, 6, 7], the comparative studies of precursor's effect on structural, optical and morphological effect is still scanty. Therefore, in present investigation, $Zn_{0.96}Cu_{0.04}O$ nanoparticles are synthesized by co-precipitation method and the role of precursors on its structural, optical and morphological properties has been discussed in detail.

2 Experimental details

2.1 Synthesis of $Zn_{0.96}Cu_{0.04}O$ nanoparticles

For the synthesis of $Zn_{0.96}Cu_{0.04}O$ nanoparticles, the analytical grade (AR), high purity chemicals (Merc, >99 %

✉ S. Muthukumaran
   drsmk123@yahoo.co.in

1   N.P.R. College of Engineering and Technology,
    Natham, Dindigul 624 401, Tamilnadu, India

2   Department of Physics, Government Arts and Science
    College, Melur, Madurai 625106, Tamilnadu, India

purity) such as zinc chloride ($ZnCl_2$), copper (II) chloride dihydrate ($CuCl_2 \cdot 2H_2O$), zinc acetate dihydrate (($CH_3COO)_2Zn \cdot 2H_2O$), copper (II) acetate monohydrate (($CH_3COO)_2Cu \cdot H_2O$), zinc nitrate hexahydrate ($Zn(NO_3)_2 \cdot 6H_2O$), copper (II) nitrate trihydrate ($Cu(NO_3)_2 \cdot 3H_2O$) and sodium hydroxide (NaOH) were used. Initially, appropriate amount of zinc chloride and copper (II) chloride dihydrate were dissolved in water and kept at constant stirring to get clear and homogeneous solution. NaOH solution had been prepared separately by dissolving appropriate amount of NaOH in 50 ml water. The prepared solution then added drop wise to the initial solution under constant stirring at room temperature and kept stirring for 2 h. The white and gelatinous precipitates were filtered and then washed several times to remove the impurities. The precipitates were dried using an oven at 80 °C for 2 h. The dried precipitates were collected and grounded using an agate mortar. Finally, the synthesized nanoparticles were annealed at 500 °C in air atmosphere for 2 h followed by furnace cooling. The same procedure was repeated to the other precursors such as acetate and nitrate.

2.2 Characterization techniques

The crystal structure of $Zn_{0.96}Cu_{0.04}O$ nanoparticles prepared using different precursors was analysed by powder X-ray diffractometer. XRD patterns were recorded by RigaKuC/max-2500 diffractometer using Cu Kα radiation ($\lambda = 1.5406$ Å) at 40 kV and 30 mA from $2\theta = 30°$ to 70°. The topological features and composition of Zn, O and Cu were determined by energy dispersive X-ray spectrometer on K and L lines. The surface morphology of $Zn_{0.96}Cu_{0.04}O$ nanoparticles were studied using a scanning electron microscope (SEM, JEOLJSM 6390). The UV–visible optical absorption study was carried out to explore their optical properties. The spectral absorption was determined using UV–visible spectrometer (Model: lambda 35, Make: Perkin Elmer) from 300 to 500 nm at ambient temperature. The presence of chemical bonding was studied by FTIR spectrometer (Model: Perkin Elmer, Make: Spectrum RX I) from 400 to 4000 cm^{-1}. The sample used for this measurement is in the form of pellets prepared by mixing the nanoparticles with KBr at 1 wt%.

The photoluminescence (PL) spectra of $Zn_{0.96}Cu_{0.04}O$ nanoparticles have been carried out between the wavelength ranging from 350 to 600 nm using a fluorescence spectrophotometer (Model: F-2500, Make: Hitachi) at room temperature. A source with a wavelength of 330 nm and power of 150 W is used as the excitation source. The magnetization (M) and magnetic hysteresis (M–H) loops were measured at room temperature using vibrating sample magnetometer (VSM, Make: Lake shore, Model: 7404).

All the characterizations were carried out at room temperature.

3 Results and discussion

3.1 X-ray diffraction (XRD): structural studies

The typical XRD spectra of $Zn_{0.96}Cu_{0.04}O$ nanoparticles prepared by various precursors like zinc chloride, zinc acetate and zinc nitrate are shown in Fig. 1. The inset of Fig. 1 shows the variation of peak intensity from 35° to 37°. The XRD spectra using zinc chloride clearly show broad peaks at the diffraction angles 31.46° (100), 34.12° (002), 35.95° (101), 47.26° (102), 56.34° (110), 62.62° (103), 66.10° (200), 67.72° (112) and 68.86° (201). The standard diffraction peaks are in good agreement with the standard JCPDS file for ZnO (JCPDS 36-1451, a = b = 3.249 Å, c = 5.206 Å) and can be indexed as the hexagonal wurtzite structure of ZnO having space group $P6_{3mc}$ with preferred orientation along (101) plane in all the samples. There are no extra peaks corresponding to Cu, oxides of Cu or Cu related phases found which insist the incorporation of Cu^{2+} instead of Zn^{2+} ions.

There is an eye-catching change in both the peak position (2θ) and the peak intensities corresponding to (101) plane. The sample prepared by zinc chloride have peak
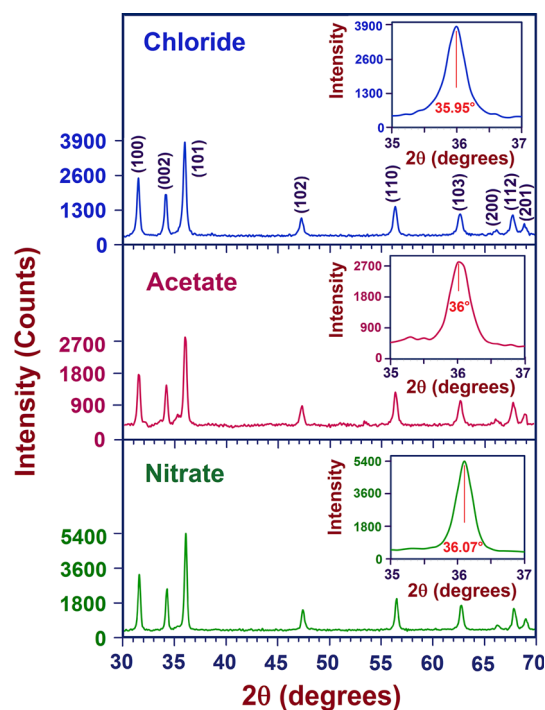

Fig. 1 Powder X-ray diffraction pattern of $Zn_{0.96}Cu_{0.04}O$ nanoparticles for different precursors like zinc chloride, zinc acetate and zinc nitrate at room temperature

position (2θ) at 35.95° which is shifted to 36.00° for Zinc acetate and 36.07° for zinc nitrate. The nanoparticles prepared by zinc nitrate exhibits higher peak intensity (5400 counts) than zinc chloride (3828 counts) and zinc acetate (2794 counts) due to the better crystallization. The average crystal size is calculated after appropriate background correction from X-ray line broadening using Debye–Scherrer's formula [8],

$$\text{Average crystallite size (D)} = \frac{0.9\,\lambda}{\beta\cos\theta} \quad (1)$$

where, λ is the wavelength of X-ray used (1.5406 Å), β is the angular peak width at half maximum in radian along (101) plane and θ is Bragg's diffraction angle. The microstrain (ε) can be calculated using the formula [8],

$$\text{Micro-strain (}\varepsilon\text{)} = \frac{\beta\cos\theta}{4} \quad (2)$$

Table 1 shows the variation of FWHM value, average crystallite size (D) and micro-strain (ε) of $Zn_{0.96}Cu_{0.04}O$ nanoparticles for different precursors. The calculated average crystallite size is low for zinc chloride precursors (22.3 nm) and high for zinc nitrate precursors (26 nm). The change of FWHM and peak intensity may be due to the size or micro-strain or size and micro-strain [1, 9]. It is noticed from Table 1 that the for zinc chloride precursors has higher strain value (0.9487×10^{-3}) than zinc nitrate (0.8147×10^{-3}) and zinc acetate (0.9032×10^{-3}). The observed low micro-strain using zinc nitrate precursor is due to the lower defects such as interstitials and vacancies than other precursors.

Table 2 shows the peak position (2θ), d-value, cell parameters 'a' and 'c', c/a ratio, stress (σ), bond length (l) and volume (V) of $Zn_{0.96}Cu_{0.04}O$ nanoparticles for different precursors. The small increase in cell parameters of $Zn_{0.96}Cu_{0.04}O$ nanoparticles compare to un-doped ZnO likely due to included impurities in the lattice. Bond length and volume of the $Zn_{0.96}Cu_{0.04}O$ nanoparticles are calculated from cell parameters by using Eqs. (3) and (4) and are tabulated in Table 2. The Zn–O bond length has been calculated using the relationship [10],

$$\text{Bond length (}l\text{)} = \sqrt{\left(\frac{a^2}{3} + \left(\frac{1}{2} - u\right)^2 c^2\right)} \quad (3)$$

where, $u = \frac{a^2}{3c^2} + 0.25$ is the potential parameter of the hexagonal structure. The volume of unit cell of hexagonal system has been calculated from the equation [11],

$$\text{Volume (V)} = 0.866 \times a^2 \times c \quad (4)$$

The stress (σ) in the ZnO plans can be determined using the following expression [12],

$$\sigma = -233 \times 10^9((C_{bulk} - C)/C_{bulk}) \quad (5)$$

where, C is the lattice constant of ZnO plans calculated from X-ray diffraction data, C_{bulk} is the strain-free lattice parameter of ZnO (5.2061 nm). It is noticed from Table 2 that the existing tensile stress is high (−2.0408 GPa) for zinc chloride precursor; low for zinc nitrate (−1.2594 GPa) and intermediate for zinc acetate (−1.6712 GPa). The negative sign indicates that the unit cells are under the state of compression. The observed low tensile stress in zinc nitrate precursor is due to the reduction of defects and lattice mismatch along c-axis. It makes the better crystallisation with lower defects which is reflected in SEM. The higher tensile stress observed in zinc chloride reduces the crystal size which leads to more defects in the lattice.

The d-value, cell parameters, bond length and volume of $Zn_{0.96}Cu_{0.04}O$ nanoparticles prepared by zinc chloride are high due to the presence of more defects. The presence of defect such as interstitial and vacancies inside the lattice leads to expansion in the lattice and thus the cell parameters, bond length and volume are high. However, these values are low for zinc nitrate precursor due to the improvement of crystal quality. The observed constant c/a ratio revealing that there is no change in hexagonal wurtzite structure by precursors. The observed low micro-strain, tensile stress, cell parameters, bond length, volume and higher peak intensities confirm that $Zn_{0.96}Cu_{0.04}O$ nanoparticles prepared using zinc nitrate have high purity and better crystallization than other precursors.

Table 1 The variation of full width at half maximum (FWHM, β) value, average crystallite size (D) and micro-strain (ε) of $Zn_{0.96}Cu_{0.04}O$ nanoparticles prepared using different precursors

Precursors	FWHM [β (°)]	Average crystallite size [D (nm)]	Micro-strain [ε (10^{-3})]
Zinc chloride	0.374	22.3	0.949
Zinc acetate	0.356	23.4	0.903
Zinc nitrate	0.320	26.0	0.815

Table 2 The variation of peak position (2θ), d-value, cell parameters 'a' and c, c/a ratio, stress (σ), bond length (l) and volume (V) of $Zn_{0.96}Cu_{0.04}O$ nanoparticles prepared using different precursors

Precursors	Peak position [2θ (°)]	d-value (Å)	Cell parameters (Å)		c/a ratio	Stress [σ (GPa)]	Bond length [l (Å)]	Volume [V (Å)³]
			a = b	c				
Zinc chloride	35.95	2.496	3.281	5.252	1.601	−2.041	1.996	48.957
Zinc acetate	36.00	2.493	3.275	5.243	1.601	−1.671	1.993	48.711
Zinc nitrate	36.07	2.488	3.269	5.234	1.601	−1.259	1.989	48.433

3.2 Scanning electron microscope (SEM) and energy dispersive X-ray spectra (EDX)

The surface morphology of $Zn_{0.96}Cu_{0.04}O$ nanoparticles using different precursors like zinc chloride, zinc acetate and zinc nitrate with different magnifications are shown in Fig. 2a–c. Figure 2a represents the SEM images of $Zn_{0.96}Cu_{0.04}O$ nanoparticles using zinc chloride precursor which are homogeneous and uniformly distributed throughout the structure. It has mixture of hexagon-like and spheroid-like particle structure in which hexagon-like structure is dominated with grain size around 15–25 nm. Figure 2b shows the surface morphology of nanoparticles using zinc acetate precursor. The mixture of spheroid-like, rod-like and the cluster form of uneven surface morphology are observed (Fig. 2c) with grain size around 20–30 nm. The presence of defects related phases are observed from Fig. 2b as discussed earlier. Figure 2c shows the mixture of agglomerated uneven spheroid-like and hexagon-like particle structure with grain size around 20–40 nm having better crystal quality than other precursors. The presence of agglomerated grains suggested that the growth process starts with the colloidal nanoclusters. The nano-clusters aggregate into larger secondary grains in order to minimize their surface energy. Then these secondary grains further collide and merge with each other to form multimers by random Brownian motion. A good correlation is found to exist between mathematical calculations from XRD and SEM studies.

Chemical purity and stoichiometry of the samples were tested by EDX spectra. The typical EDX spectra of $Zn_{0.96}Cu_{0.04}O$ nanoparticles prepared using zinc chloride, zinc acetate and zinc nitrate precursors are as shown in Fig. 3a–c. The quantitative atomic percentage of the compositional elements such as Zn, Cu and O present in $Zn_{0.96}Cu_{0.04}O$ nanoparticles under different precursors are given in insert of Fig. 3. The EDX analysis confirms the presence of Cu in ZnO and purity of system. It is observed from Fig. 3a–c that the atomic percentage is derived to be 4.57, 4.54 and 4.26 % for zinc chloride, zinc acetate and zinc nitrate precursors, respectively. The atomic percentage is nearly equal to their nominal stoichiometry within the experimental error. The atomic percentage of zinc is high (at.% = 39.06) for the samples prepared using zinc nitrate precursor than zinc acetate (at.% = 37.97) and zinc chloride (at.% = 32.75). However, the presence oxygen is low in zinc nitrate than other precursors. The above behaviours support the existence of lower defects in zinc nitrate precursor.

3.3 UV–visible spectra: optical studies

The UV–visible optical absorption spectra of $Zn_{0.96}Cu_{0.04}O$ nanoparticles prepared using different precursors have been carried out at room temperature using UV–visible spectrometer (Model: Lambda 35, Make: Perkin Elmer) from 300 to 500 nm and shown in Fig. 4. The inset of Fig. 4 shows the enlarged and clear picture of the absorption changes from 300 to 360 nm.

The $Zn_{0.96}Cu_{0.04}O$ nanoparticles prepared using zinc nitrate has high and broad band absorption in UV region than other precursors. In general, number of crystal and crystal size plays important role in the optical absorption and transmittance process. The number of crystal and its size is high for zinc nitrate precursor. Since it has larger crystal size, the presence of absorption centres is also high. Therefore, the observed high absorption of $Zn_{0.96}Cu_{0.04}O$ nanoparticles prepared using zinc nitrate is due to its high crystal size. Immediately after UV region (visible region), the magnitude of absorption is almost zero and shows opposite to that of UV region. However, the observed low absorption in UV region and higher absorption in visible region for zinc chloride precursor than zinc nitrate is due to its low crystal size. The absorption peak for Zinc nitrate precursor is 307 nm which is shifted to 311 nm for zinc acetate precursor and 323 nm for zinc nitrate precursor. The change of absorption peak by precursors is due to the size effect.

The typical room temperature transmittance spectra of $Zn_{0.96}Cu_{0.04}O$ nanoparticles prepared using different precursors are shown in Fig. 5. Even though the transmittance spectra show just opposite trend of the optical absorption
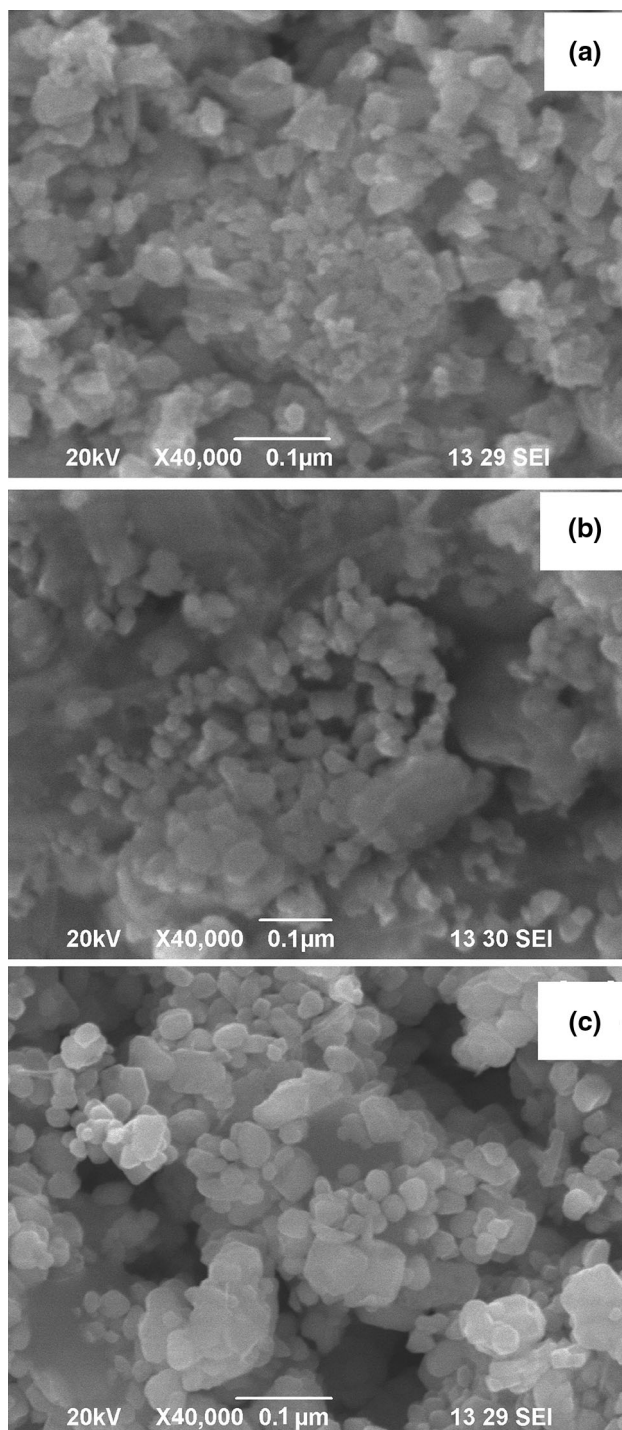
Fig. 2 Scanning electron microscope (SEM) images of $Zn_{0.96}Cu_{0.04}O$ nanoparticles using different precursors. **a** Zinc chloride, **b** zinc acetate and **c** zinc nitrate at room temperature

Fig. 3 Energy dispersive X-ray (EDX) spectra of $Zn_{0.96}Cu_{0.04}O$ nanoparticles for different precursors. **a** Zinc chloride, **b** zinc acetate and **c** zinc nitrate at room temperature. The *inset* shows the quantitative weight and atomic percentage of the compositional elements

spectra, it explores some additional features which are not seen in absorption spectra. Zinc nitrate precursor has relatively low magnitude but broad transmittance band in UV region and stronger transmittance in the visible region
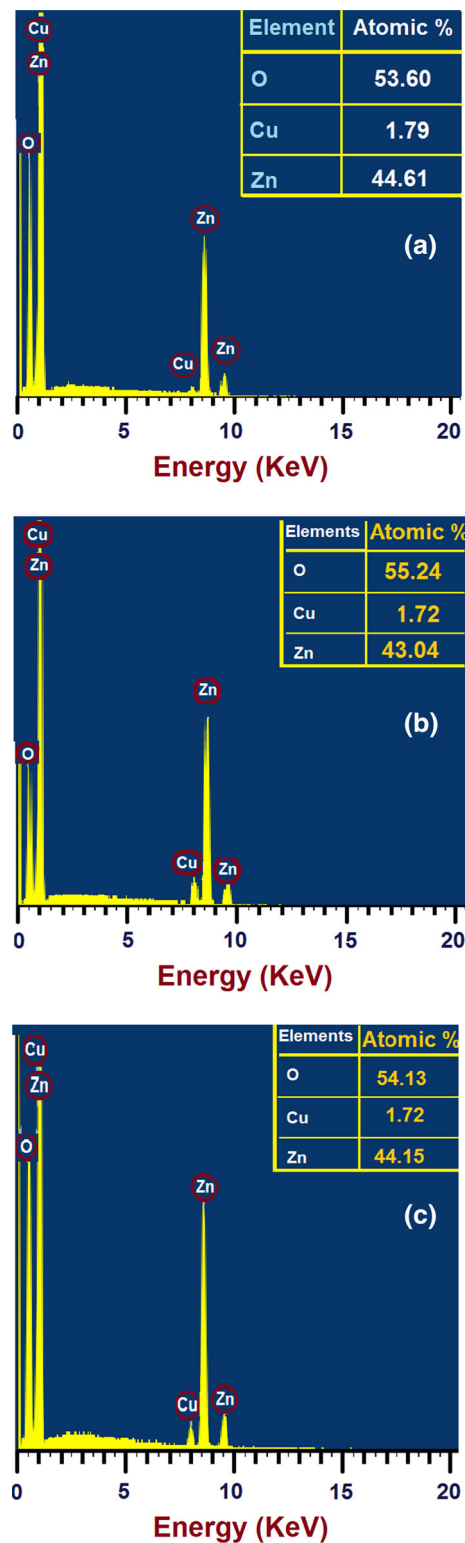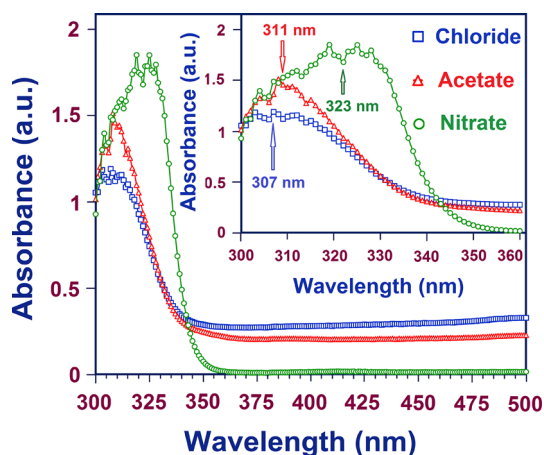
Fig. 4 UV–visible absorption spectra of $Zn_{0.96}Cu_{0.04}O$ nanoparticles for different precursors as a function of wavelength from 300 to 500 nm. The *inset* shows the high resolution absorption spectra from 300 to 360 nm
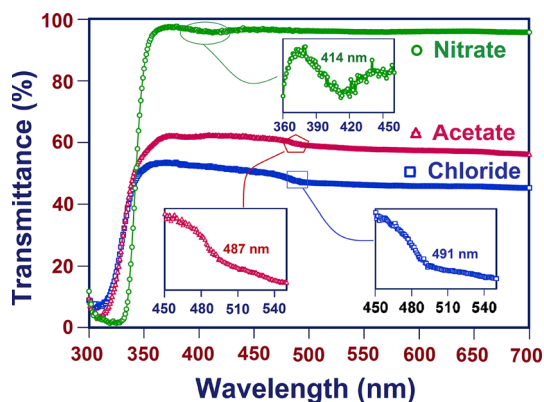

Fig. 5 Transmittance spectra of precursors, zinc chloride, zinc acetate and zinc nitrate at room temperature. The *inset* shows the high resolution spectra from 360 to 450 nm for zinc nitrate precursor and 450–550 nm for zinc acetate and zinc nitrate precursors

compared to the other precursors. The strong and transparent behaviour in the visible region of the sample using zinc nitrate precursor strongly insist the existence of less defects and enhanced crystal size. The higher transmittance (almost 100 %) leads to the industrial applications especially as transparent electrode. However, the observed weak transmittance in the sample using zinc chloride precursor is due to large defect. The presence of more defects increases the absorption in visible region via the level formed by defect and hence reduces the transmittance.

The inset of Fig. 5 shows the clear picture of absorbance between 360 and 450 nm for zinc nitrate precursor and 450–550 nm for both zinc acetate and zinc chloride precursors. A weak and broad absorption band is observed around 414 nm (corresponding to blue band) for zinc nitrate precursor which is shifted to lower wavelength side

(blue shift) below 400 nm for other two precursors with decreasing transmittance. The present blue shift could be ascribed by the formation of new emission centres [13]. Defect related emission in the visible region was already discussed in the literature [14, 15]. The peak corresponding to 414 nm is originated due to the intrinsic defects the interstitial position of Zn^{2+} ion [16]. The change in blue band intensity is due the interstitial of Zn^{2+} ions which is in good agreement with the EDX results. According to Sun et al. [17], the blue emission is corresponding to the relaxation from the excited electrons from the level of interstitial Zn (Zn_i) to extended Zn_i states and transit to the valence band with the emission of blue emission. The observed green band around 487 nm for zinc acetate precursor and 491 nm for zinc chloride are the oxygen vacancies and intrinsic defects [18]. Previous literature suggested that Cu-doped ZnO can produce the absorption near the green band [2]. Since the absorption corresponding to the defect related green band is not seen in zinc nitrate precursor, it is concluded that the existence of defects and defects related phases are very low.

The optical band gap is evaluated using the Tauc relation [6]:

$$h\upsilon = A\left(h\upsilon - E_g\right)^n \tag{6}$$

where, A as a constant, E_g is optical band gap of the material and the exponent n depends upon the type of transition. The values of n for direct allowed, indirect allowed and direct forbidden are 1/2, 2, 3/2. In the present case, n is taken as 1/2.

The optical energy band gap (E_g) can be estimated by plotting $(\alpha h\upsilon)^2$ versus the photon energy $h\upsilon$ in the fundamental absorption region as shown in Fig. 6. Extrapolation of linear portion to the energy axis at $(\alpha h\upsilon)^2 = 0$ gives the energy gap (E_g) value. The energy gap is varied between 3.65 and 3.75 eV, where zinc nitrate precursor has

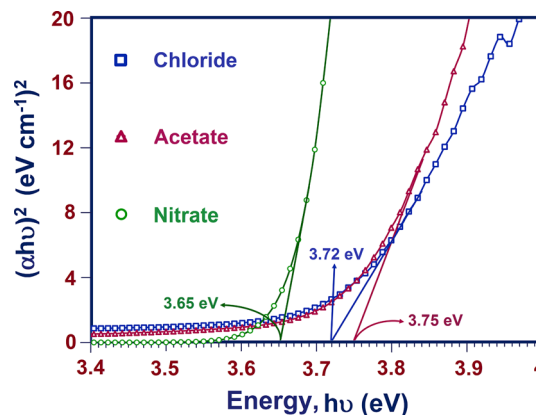**Fig. 6** The $(\alpha h\upsilon)^2$ versus $h\upsilon$ curves of $Zn_{0.96}Cu_{0.04}O$ nanoparticles for different precursors for the optical energy gap calculation

$E_g = 3.65$ eV (minimum) and zinc acetate precursor has $E_g = 3.75$ eV (maximum). The observed higher energy gap in zinc chloride precursor could be attributed to the poor crystallinity of the nanoparticles and also the formation of the new compound based on Cu and Zn [19]. During the preparation of nanoparticles using zinc nitrate precursor, the residual electrons originated from Cu-doping could re-strain the formation of defects. The reduction in strain and the better crystallinity effectively depress interstitial defects like O_i and Zn_i. The decrease in the optical band gap for zinc nitrate precursor can be attributed to the better crystallinity with increasing grain size. If Cu is located at substitution sites, the carrier concentration is increased and consequently the band gap is reduced which could be due to the Moss–Burstein effect [20]. Wang et al. [21] discussed that both compositional and size effect are responsible for the band gap variation. They also noticed that the band gap is decreased with the increase of average crystallite size. In the present work, there is no change in composition. Therefore, the change in energy gap is due to crystal size.

3.4 Fourier transform infrared (FTIR) studies

The characteristic peaks exhibited by FTIR spectra of $Zn_{0.96}Cu_{0.04}O$ nanoparticles prepared using different precursors are shown in Fig. 7a. Figure 7b shows the enlarged FTIR spectra below 1000 cm^{-1}. The IR frequencies along with the vibrational assignments of the samples assigned at room temperature are listed in Table 3. The broad absorption peaks around 2700–3500 cm^{-1} are attributed to normal polymeric O–H stretching vibration of H_2O in Cu–Zn–O lattice [22] which may be due to moisture in the solution and the atmosphere. Another sharp peak around 1637–1642 cm^{-1} is attributed to H–O–H bending vibration, which is assigned to a small amount of H_2O in the ZnO nanocrystals [1]. The principal absorption peaks observed between 1394 and 1436 cm^{-1} are corresponding to the asymmetric and symmetric stretching of carboxyl group (C=O) [23]. The absorption peaks observed between 2334 and 2348 cm^{-1} are because of the existence of CO_2 molecule in air [23].

The IR peaks below 1000 cm^{-1} (Fig. 7b) is used to predict the presence or absence of Zn–O/Cu–O/Zn–O–Cu bonds. In general, the characteristic peaks between 420 and 620 cm^{-1} corresponding to the stretching vibration modes of ZnO [24]. The medium to weak bands at 626 and 762 cm^{-1} in zinc chloride precursor are assigned to the vibrational frequency of Zn–Cu–O local bond in Zn–O lattice [6]. The Zn–O bond is assigned to the stretching frequency at 451 cm^{-1}. The medium to weak bands at 620 cm^{-1} in zinc acetate precursor is assigned to the vibrational frequency of Zn–Cu–O local bond and the
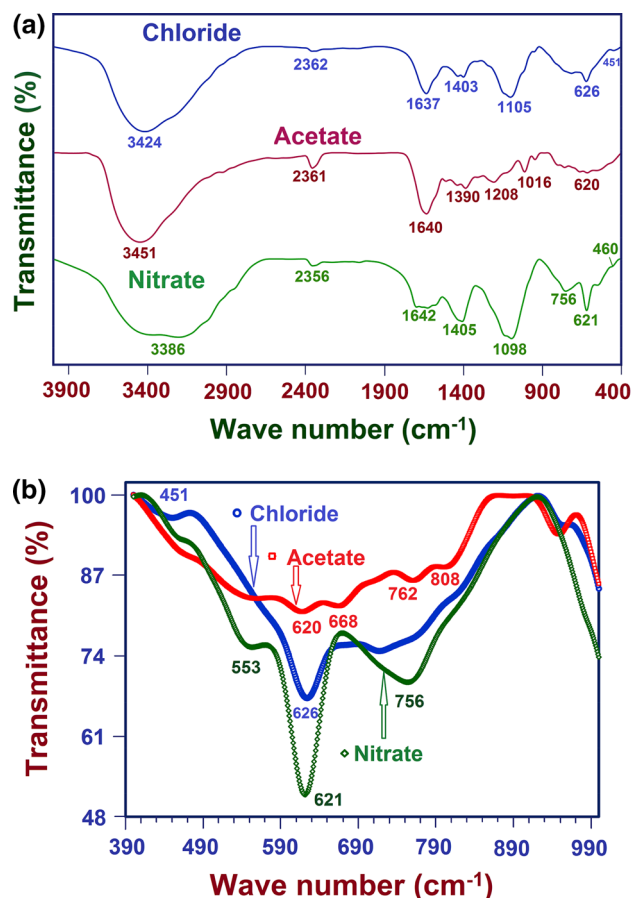

Fig. 7 **a** FTIR spectra of $Zn_{0.96}Cu_{0.04}O$ nanoparticles for different precursors from 400 to 4000 cm^{-1} at room temperature and **b** the enlarged FTIR spectra <1000 cm^{-1}

additional weak bands at 668, 762 and 808 cm^{-1} represents defect states surrounding to Cu^{2+} ions. The characteristic peak around 550 cm^{-1} is assigned to Zn–O stretching frequency. The Zn–O bond is assigned to the stretching frequency at 553 cm^{-1} for zinc nitrate precursor. The medium to strong bands than other precursor at 621 and 756 cm^{-1} represents the vibrational frequency of Zn–Cu–O local bond in Zn–O lattice.

3.5 Photoluminescence (PL) spectra

Potential applications such as laser devices, light emitting diodes and optical sensing devices make great interest on luminescence properties of Cu-doped ZnO. Room temperature PL spectra of $Zn_{0.96}Cu_{0.04}O$ nanoparticles prepared using different precursors such as zinc chloride, zinc acetate and zinc nitrate are as shown in Fig. 8. All the samples contain four different bands between 350 and 600 nm. First band around 388 nm corresponding to UV region and other bands arising from the deep level emission in visible region.

Table 3 IR peaks and their assignments of $Zn_{0.96}Cu_{0.04}O$ nanoparticles prepared using different precursors

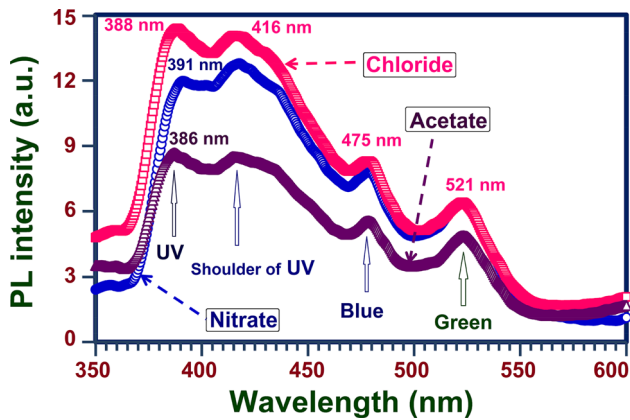| Assignments	Wave number (cm^{-1})		
	Zinc chloride	Zinc acetate	Zinc nitrate
O–H stretching vibration of H_2O	3424	3451	3386
CO_2 stretching vibration	2362	2361	2356
C=O stretching vibration	1403	1390	1405
H–O–H bending vibration	1637	1640	1642
Stretching mode of Zn–O	626	620	621

Fig. 8 Room temperature PL spectra of $Zn_{0.96}Cu_{0.04}O$ nanoparticles for different precursors from 350 to 600 nm

The UV emission around 388 nm arises from the recombination of free excitons and is commonly known as near band edge (NBE) transition of ZnO [1]. The intensity of UV emission is high for zinc chloride precursor and it is low for zinc acetate. The moderate UV intensity for nitrate precursor is responsible for its better crystallization. The suppression of excitonic emission (UV emission) at zinc acetate precursor is due to the increase of defect related non-radiative recombination centres [25]. The broad and weak band between 413 and 419 nm, named as shoulder of UV emission, is due to the transition of excitons from shallow donor level (Zn_i) which lies below the conduction band to the valance band [26]. The observed blue band around 475 nm may be due to the transition between shallow donor levels (Zn_i) and shallow accepter levels (V_{zn}). The oxygen vacancies generated by Cu-doping in ZnO lattices [27] is responsible for the noticed green emission band around 521 nm.

Figure 9 shows the magnified room temperature PL spectra of $Zn_{0.96}Cu_{0.04}O$ nanoparticles prepared using different precursors between 450 and 550 nm. The change in intensity ratio between green band and blue band (I_G/I_B ratio) is given as inset of Fig. 9. The I_G/I_B ratio is almost same for (0.83 for zinc chloride and 0.87 for zinc nitrate) chloride and nitrate. It is high and almost equal to one (0.92) for zinc acetate precursor. The higher value implies
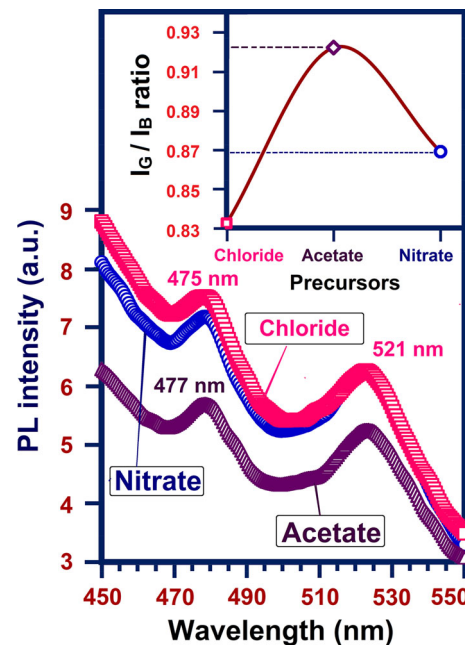

Fig. 9 Magnified PL spectra of $Zn_{0.96}Cu_{0.04}O$ nanoparticles for different precursors from 450 to 550 nm. The *inset* shows the intensity ratio between *green* band and *blue* band (I_G/I_B ratio) for different precursors (Color figure online)

that $Zn_{0.96}Cu_{0.04}O$ nanoparticles prepared using zinc acetate precursor creates large number of defects inside the lattice and consist of higher defect density.

3.6 Magnetic properties

The room temperature magnetic properties of Cu-doped ZnO nanoparticles have been studied by vibrating sample magnetometer (VSM). Figure 10a–c shows the magnetization versus magnetic field (M–H) hysteresis loops of $Zn_{0.96}Cu_{0.04}O$ nanoparticles with different precursors such as zinc chloride, zinc acetate and zinc nitrate which reveal the ferromagnetic behaviour for all the samples.

Room temperature ferromagnetic (RTFM) nature of $Zn_{0.96}Cu_{0.04}O$ sample with nitrate precursor is shown in Fig. 10a. There could be several possible reasons for RTFM in $Zn_{0.96}Cu_{0.04}O$ nanoparticles. Doping of p-type
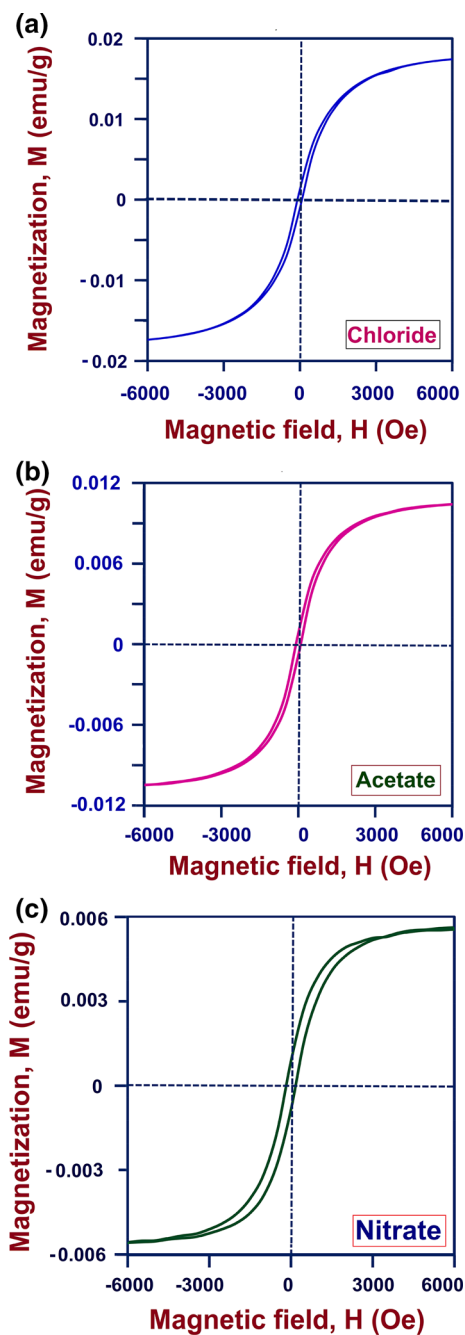
(a)

(b)

(c)

Fig. 10 Magnetization versus magnetic field (M–H) curves $Zn_{0.96}$ $Cu_{0.04}O$ nanoparticles for **a** zinc chloride, **b** zinc acetate and **c** zinc nitrate at room temperature

Cu into ZnO is the main reason for RTFM [28]. Cao et al. [29] explained that the important reason to induce RTFM is p-type carriers generated by Cu doping. Xia et al. [15] described that the RTFM noticed in Cu-doped ZnO is due to the exchange interaction between local spin-polarized electrons and conductive electrons as explained by Ruderman–Kittel–Kasuya–Yosida (RKKY) theory. The point defects such as Zn interstitial/oxygen vacancies [30] or

segregation of secondary phases/metallic clusters are the other possible reasons for RTFM. In the present case, no extra peaks corresponding to secondary phases like CuO, Cu_2O or Cu cluster detected in XRD studies. Moreover, Cu related secondary phases exhibit antiferromagnetic nature above room temperature [31]. Therefore, the RTFM observed in Cu doped ZnO is not by any secondary phases or Cu clusters and is intrinsic.

Sample with zinc chloride precursor has higher magnetization than other samples where the samples with acetate and nitrate precursors have more or less same magnetization. The present suppressed magnetization is explained based on the structural parameters of the nanoparticles. Since, the samples with acetate and nitrate precursors have smaller lattice volume than the sample with chloride (Fig. 10), the relative distance between neighbouring Cu–Cu pair decreases. The decrease of relative distance between Cu–Cu accelerate the antiferromagnetic coupling [32] which suppress the ferromagnetic order as predicted by earlier literature [33]. In addition, higher volume of the sample with chloride precursor is also responsible for its higher magnetization. The similar trend of magnetization based on lattice volume was explained by Ahmed et al. [34].

4 Conclusion

$Zn_{0.96}Cu_{0.04}O$ nanoparticles are successfully synthesized by co-precipitation method using various precursors like zinc chloride, zinc acetate and zinc nitrate. The XRD spectra showed that the prepared nanoparticles have different microstructure without changing a hexagonal wurtzite structure. The calculated average crystallite size from XRD spectra was low for zinc chloride precursors (22.3 nm) and high for zinc nitrate precursors (26 nm). The strong and transparent behaviour in the visible region of the sample using zinc nitrate precursor strongly insist the existence of less defects and enhanced crystallite size which leads to the industrial applications especially as transparent electrode. The reduction in strain and the better crystallinity effectively depress interstitial defects. The energy gap is varied between 3.65 and 3.75 eV, where zinc nitrate precursor has $E_g = 3.65$ eV (minimum) and zinc acetate precursor has $E_g = 3.75$ eV (maximum). The observed higher energy gap using zinc chloride precursor could be attributed to the poor crystallinity and also the formation of the new compound based on Cu and Zn. The low energy gap for zinc nitrate precursor can be attributed to the better crystallinity with increasing grain size. Change in luminescence intensity and magnetization were discussed based on the defects created precursors.

References

1. A. Jagannatha Reddy, M.K. Kokila, H. Nagabhushana, R.P.S. Chakradhar, C. Shivakumara, J.L. Rao, B.M. Nagabhushana, J. Alloys Compd. **509**, 5349 (2011)
2. N.Y. Garces, L. Wang, L. Bai, N.C. Giles, L.E. Halliburton, G. Cantwell, Appl. Phys. Lett. **81**, 622 (2002)
3. P. Fons, A. Yamada, K. Iwata, K. Matsubara, S. Niki, K. Nakahara, H. Takasul, Nucl. Instrum. Methods Phys. Res. B **199**, 190 (2003)
4. M. Ferhat, A. Zaoui, R. Ahuja, Appl. Phys. Lett. **94**, 142502 (2009)
5. Y. Wei, D. Hou, S. Qiao, C. Zhen, G. Tang, Phys. B **404**, 2486 (2009)
6. S. Muthukumaran, R. Gopalakrishnan, Opt. Mater. **34**, 1946 (2012)
7. H. Liu, J. Yang, Z. Hua, Y. Zhang, L. Yang, L. Xiao, Z. Xie, Appl. Surf. Sci. **256**, 4162 (2010)
8. S. Muthukumaran, R. Gopalakrishnan, Phys. B **407**, 3448 (2012)
9. J. Pelleg, E. Elish, J. Vac. Sci. Technol. A **20**, 754 (2002)
10. B.D. Cullity, *Elements of X-ray Diffractions* (Addison-Wesley, Reading, MA, 1978)
11. G. Srinivasan, R.T.R. Kumar, J. Kumar, J. Sol-Gel. Sci. Technol. **43**, 171 (2007)
12. O. Lupan, T. Pauporte, L. Chow, B. Viana, F. Pelle, L.K. Ono, B.R. Cuenya, H. Heinrich, Appl. Surf. Sci. **256**, 1895 (2010)
13. H. Zheng, J.L. Song, Q. Jiang, J.S. Lian, Appl. Surf. Sci. **258**, 6735 (2012)
14. J. Zhang, L. Sun, J. Yin, H. Su, C. Liao, C. Yon, Chem. Mater. **14**, 4172 (2002)
15. C.H. Xia, C.G. Hu, C.H. Hu, Z. Ping, F. Wang, Bull. Mater. Sci. **34**, 1083 (2011)
16. M.H. Huang, Y.Y. Wu, H.N. Feich, N. Tran, E. Weber, P.D. Yang, Adv. Mater. **13**, 113 (2001)
17. Y.M. Sun, Study on the synthesis and physical properties of ZnO-based diluted magnetic semiconductors. Ph.D. thesis, University of Science and Technology of China, 2000
18. C. Li, G. Fang, Q. Fu, F. Su, G. Li, X. Wu, X. Zhao, J. Cryst. Growth **292**, 19 (2006)
19. M. Öztas, M. Bedir, Thin Solid Films **516**, 1703 (2008)
20. E. Burstein, Phys. Rev. **93**, 632 (1954)
21. Y. Wang, G. Ouyang, L.L. Wang, L.M. Tang, D.S. Tang, C.Q. Sun, Chem. Phys. Lett. **463**, 383 (2008)
22. K. Nakamoto, *Infrared and Raman Spectra of Inorganic and Coordination Compounds, Parts-A and B* (Wiley, New York, 1997)
23. S. Senthilkumaar, K. Rajendran, S. Banerjee, T.K. Chini, V. Sengodan, Mater. Sci. Semi. Process **11**, 6 (2008)
24. H. Kleinwechter, C. Janzen, J. Knipping, H. Wiggers, P. Roth, J. Mater. Sci. **7**, 4349 (2002)
25. M. Deepa, N. Bahadur, A.K. Srivastava, P. Chaganti, K.N. Sood, J. Phys. Chem. Solids **70**, 291 (2009)
26. W.J. Qin, J. Sun, J. Yang, X.W. Du, Mater. Chem. Phys. **130**, 425 (2011)
27. S.B. Zhang, S.H. Wei, A. Zunger, Phys. Rev. B **63**, 075205 (2001)
28. L.H. Ye, A.J. Freeman, B. Delley, Phys. Rev. B **73**, 033203 (2006)
29. P. Cao, D.X. Zhao, D.Z. Shen, J.Y. Zhang, Z.Z. Zhang, Y. Bai, Appl. Surf. Sci. **255**, 3639 (2009)
30. T.S. Herng, S.P. Lau, S.F. Yu, J.S. Chen, K.S. Teng, J. Magn. Magn. Mater. **315**, 107 (2007)
31. P. Thakur, V. Bisogni, J.C. Cezar, N.B. Brookes, G. Ghiringhelli, S. Gautam, K.H. Chae, M. Subramanian, R. Jayavel, K. Asokan, J. Appl. Phys. **107**, 103915 (2011)
32. G.J. Huang, J.B. Wang, X.L. Zhong, G.C. Zhou, H.L. Yan, J. Mater. Sci. **42**, 6464 (2007)
33. T.S. Herng, S.P. Lau, S.F. Yu, H.Y. Yang, X.H. Ji, J.S. Chen, N. Yasui, H. Inaba, J. Appl. Phys. **99**, 086101 (2006)
34. F. Ahmed, S. Kumar, N. Arshi, M.S. Anwar, S.N. Heo, B.H. Koo, Acta Mater. **60**, 5190 (2012)